





Online Pressure Map Reconstruction in a Multitouch Soft Optical Waveguide Skin

Matteo Lo Preti , Massimo Totaro, *Member, IEEE*, Egidio Falotico , *Member, IEEE*, Marco Crepaldi , *Member, IEEE*, and Lucia Beccai , *Member, IEEE*

Abstract—In this article, we present a reconstruction method for mapping a wide range of pressure stimuli in a multitouch soft optical waveguide skin (MSOWS). Distributed sensing information is typically obtained from wired soft sensing units. This approach hardly adapts to different shapes and has limited durability against stresses and shocks. In our MSOWS, the spatial tactile transduction relies on a continuum sensitive area of graded-stiffness polydimethylsiloxane, with a virtual grid free from electronics and connections. The sensing range of each cell is up to 234 kPa, and the spatial resolution is 5 mm. We use a time-delay neural network to reduce the hysteresis of the soft material to less than 1%. In addition, a fault-tolerant mechanism makes the entire system robust to component failure. These results may open the way to a new generation of distributed soft skins that are versatile due to material design and processing.

Index Terms—Machine learning, multi-touch, online reconstruction, optical waveguide, soft skin.

I. INTRODUCTION

DISTRIBUTED sensing is critical for building intelligent artificial systems, such as those for robotic manipulation [1]–[3], human–robot interaction [4], [5], and healthcare [6], [7]. In the aforementioned applications, physical sensing by touch is essential, and perception demands gathering tactile information in real time (RT) at several points at the same time and, possibly, with redundancy. In robotics, distributed sensorization has been mainly achieved by modular structures or arrays [8] with rigid components/materials. Alternatively,

ultrathin and conformable electronic skins (e-skins) have been demonstrated for wearable and skin-attachable systems [9]. Indeed, in soft electronic systems, stresses concentrate at soldering points of connectors and wirings, since they are typically the most rigid parts of the structure. If these elements have an array-like structure, they cannot conform well to surfaces they have not been designed for. Furthermore, soft systems may undergo large deformations, and their repeated actions will inevitably compromise the signal flow. Moreover, e-skins hardly adapt to different shapes, and their wirings and interconnections scale quadratically with the covered surface, which increases hardware complexity in robotic systems and drastically reduces the reliability in wearables and skin-mounted arrays. A possible solution is to avoid a one-to-one correspondence between sensing elements and taxels by introducing appropriate learning-based signal processing strategies. Therefore, new algorithms that can handle complex and large datasets are needed to implement distributed sensing with simple wiring and reduced taxels.

As it will be described in the following, such signal processing strategies hold a great potential when coupled with transduction methods that enable spatial tactile transduction without relying on physical layouts of distributed sensing units, i.e., a system with rigid electronic components arranged within a grid. One remarkable achievement in this direction has been obtained by Hellebrekers *et al.* [10].

Soft tactile sensors perceive mechanical stimuli by exploiting the mechanical properties of compliant interfaces [11]. From the technological point of view, different transduction strategies have been widely investigated, i.e., piezoresistive [12]–[15], capacitive [16]–[18], inductive [19], [20], and optoelectronic [21]–[24]. An overview of their characteristics can be found in **Table I** [25]–[29]. Among them, optical sensors have attractive characteristics, such as a broad sensitivity range, high reliability, and low susceptibility to electromagnetic interference. Moreover, even though materials must be optically clear and elastic, the resulting sensitive area is free from wires or rigid components. This is a clear advantage for intelligent tactile systems that need to morphologically adapt to the environment.

In soft optical sensing, point-to-point or distributed sensing approaches can be addressed. A typical example of the first case is the soft optical lace (or fiber) waveguide, in which a photoemitter (PE) and the corresponding photoreceiver (PR) are located at each opposite end. Here, the optical signal travels in the direction specified by the lace itself, and the sensitive region lies between the two optical components. Thus, there

Manuscript received 19 July 2021; revised 20 November 2021 and 8 February 2022; accepted 8 March 2022. Date of publication 5 April 2022; date of current version 14 December 2022. Recommended by Technical Editor H. Xie and Senior Editor H. Qiao. This work was supported by European Union's Horizon 2020 Program under Grant 863212 PROBOSCIS. (*Corresponding author: Matteo Lo Preti.*)

Matteo Lo Preti is with the Istituto Italiano di Tecnologia, 16163 Genova, Italy, and also with the Biorobotics Institute, Scuola Superiore Sant'Anna, 56025 Pontedera, Italy (e-mail: matteo.lopreti@iit.it).

Massimo Totaro, Marco Crepaldi, and Lucia Beccai are with the Istituto Italiano di Tecnologia, 16163 Genova, Italy (e-mail: massimo.totaro@iit.it; marco.crepaldi@iit.it; lucia.beccai@iit.it).

Egidio Falotico is with the Biorobotics Institute, Scuola Superiore Sant'Anna, 56025 Pontedera, Italy, and also with the Department of Excellence in Robotics and AI, Scuola Superiore Sant'Anna, 56125 Pisa, Italy (e-mail: egidio.falotico@santannapisa.it).

This article has supplementary material provided by the authors and color versions of one or more figures available at <https://doi.org/10.1109/TMECH.2022.3158979>.

Digital Object Identifier 10.1109/TMECH.2022.3158979

TABLE I

COMPARISON OF THE CHARACTERISTICS OF SOFT SENSORS BASED ON THE TRANSDUCTION PRINCIPLE

	Piezoresistive [12], [14]	Capacitive [16], [18]	Inductive [19], [20]	Optical [21], [24]
Dynamic Range	●●○	●●○	●●●●	●●●●
Spatial Resolution	●●●	●●○	●○○	●●●
Sensitivity	●●○	●●○	●●●●	●●○
Linearity	●○○	●●○	●●●●	●●○
Physical Robustness	●●○	●○○	●●○	●●○
Complexity	●○○	●●●●	●●●●	●●○
Wirings	●●○	●●●●	●●○	●○○
Noise	●●○	●●●●	●●○	●○○
Temperature sensitivity	●●●	●○○	●●●●	●●○
Hysteresis	●●●	●●●●	●○○	●●○
Drift	●●●	●○○	●●○	●○○
Power Consumption	●○○	●○○	●●●●	●●●●
Cost	●○○	●○○	●●○	●●○

Positive characteristics are reported in green, and negative in red. The best score is either three green marks or one red mark.

is a direct correspondence between the PE–PR couple (or the lace itself) and an applied stimulus. For example, Rossiter and Mukai [23] presented an optical-based tactile skin, in which LEDs are mounted back to back in pairs to retrieve the applied force and position. Different architectures can be implemented by using bundles of soft laces. Remarkably, Xu *et al.* [22] extended the concept of soft sensing using optical lacings to achieve a sensorized 3-D structure. However, this kind of sensing is prone to interferences and losses between fibers when either the number of stimuli increases or the sensor scales up. Contrary to the point-to-point case, the sensitive area of a continuum soft optical waveguide is delimited by many PEs and PRs at its contour [30]. In this case, a pair of optical components has no direct correspondence with a tactile stimulus. Therefore, the detection of distributed tactile information is only possible by introducing effective data processing methods. A significant advantage of this approach is to retrieve spatial information from an extended region that is entirely free of wiring or electronic components and can be designed with different shapes, which could facilitate hardware integration into robotic systems in the future.

This article focuses on the tactile reconstruction process, which is crucial for the development of a soft optical waveguide skin [31] able to detect tactile information in RT.

The reconstruction of a pressure map in a system without electronics in the sensing area is an ill-posed nonlinear inverse problem. To date, there have been few methods in the literature, and there is no common framework to evaluate the performance of the reconstructions. Contact map reconstructions are generally evaluated using the Euclidean distance [32] or mean squared error (MSE) [33], [34]. However, these metrics have generic purpose, and a specific indicator for pressure map evaluation is still missing.

Adler *et al.* [35] proposed a method to evaluate the performance of electrical impedance tomography (EIT)-based algorithms given a forward model. Nevertheless, it is not uncommon that a forward model is not available or that the reconstruction is based on an EIT-based algorithm only. When any of these conditions occur, the method cannot be applied.

Machine learning has been widely used in the context of tactile reconstruction. It is the automated process of pattern extraction from data [36], and one of its applications can be single-touch reconstruction. Supervised learning [37] can map the relationship between input data and contact location [32], [33], [38]. A new kind of versatility is introduced: different data sources (e.g., conductive, optical, resistive, and fluidic) can be used with minimal changes in the network architecture. Once trained, single-touch reconstruction can achieve high accuracies and fast response time. Different networks can be trained to retrieve different pieces of information: for instance, Amoateng *et al.* [39] used one network for single-touch reconstruction and another for pressure-level regression. Despite these promising results, there are still many open challenges. For example, how to deal with spatiotemporal nonlinearities of soft systems and how to properly train general machine learning models [40]. Another challenge in distributed sensors is the transition from single-touch to multitouch, since data-driven methods require large amounts of training data [41]. In fact, multitouch requires training data from the combinations of multiple contact points [42]. Not only would the method be time-consuming and computationally intensive, but it may also become impractical as the number of contact points increases [41]. EIT-based algorithms are extensively adopted. EIT-based sensors use boundary electrodes to obtain the conductivity distribution of the sensing region associated with pressure excitations. The main advantages of this method are the simplicity of the structure and low cost. However, it lacks temporal resolution, the computational cost is high, and the output is strongly influenced by the arrangement of the electronic components [30], [43], [44]. The reconstruction is severely affected by artifacts. This bottleneck has been addressed by optimizing the solution of the inverse problem with additional processing steps. For instance, the algorithm developed by Liu *et al.* [45] is designed to solve a shape-reconstruction problem with prior knowledge about the objects to be identified. However, the effectiveness of the reconstruction is heavily biased by this prior information. Block sparse Bayesian learning (BSBL) [46] has been widely studied for its robustness to noise. Remarkably, Liu *et al.* [47] improved the reconstruction quality with structure-aware BSBL. Another trend is the application of deep learning to EIT [48], using algorithms like the U-net [34], [49].

Herein, we address the above challenges and demonstrate the reconstruction of tactile information for distributed sensing in a soft optical waveguide skin. We propose a data processing workflow to retrieve an online and multitouch pressure map with adaptive hysteresis compensation [50], [51] and fault tolerance in a graded-stiffness (GS) waveguide skin. The considerations on the design and geometry of the substrate are addressed in Section II-A. The system and the experimental setup are explained in Section II-C. The algorithms for the multitouch, pressure estimation, fault tolerance, and hysteresis compensation are

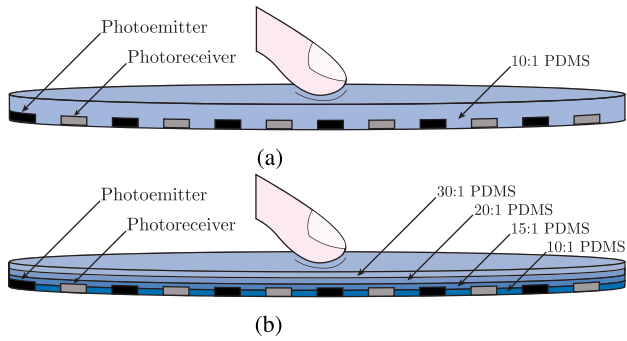


Fig. 1. Sketches of the SL and GS MSOWS. The PEs and PRs are reported in black and gray, respectively. (a) SL skin. (b) GS skin.

described in Section II-D. Finally, the developed performance evaluation method is explained in Section II-E.

II. MATERIALS AND METHODS

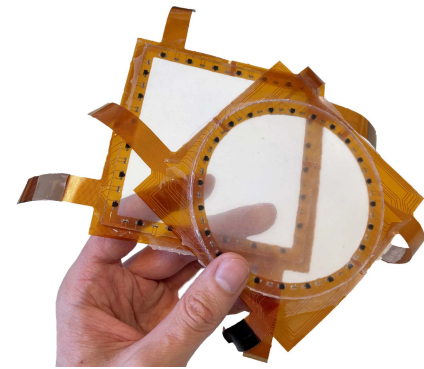
A. Design of Multitouch Soft Optical Waveguide Skin (MSOWS)

The soft waveguide skin approach to tactile sensing was experimented for the first time by our group [30], [39] and is based on the principle of frustrated total internal refraction [52]. Near-infrared (NIR) light is held within an elastomeric layer of polydimethylsiloxane (PDMS) (Dow Corning, Sylgard 184, with a refractive index of 1.42), which acts as both mechanical substrate and waveguide. In the prototypes developed for this work, 24 PEs illuminate the substrate volume, while 24 PRs detect changes in light amplitude. The peak of emission of the PEs (infrared LEDs, VSMY1850) is at 850 nm and matches the peak of reception of the PRs (silicon NPN epitaxial planar detectors, VEMT2023SLX01). Both the circular and square prototypes were fabricated (as shown in Fig. 2), with a diameter/side of 47 mm and a height of 4 mm. Flexible printed circuit boards (PCBs) were designed accordingly to cover 1/4 of the boundary each. These two shapes have significant differences in the way rays are spread. Indeed, the sharp corners of the square can be seen as the limit case of round corners of the circular geometry.

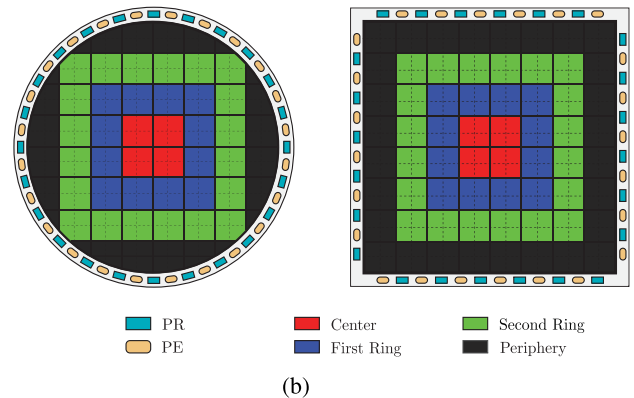
Each PCB integrates six PEs and six PRs in an alternating manner. Thus, the selected shapes were obtained by assembling four PCBs in the desired final shape (circular or square) and connecting them to the data acquisition (DAQ) board. Therefore, the sensing area is free of rigid elements, wires, or connections. It is noteworthy that the number of components in such a soft waveguide approach scales linearly with the perimeter rather than quadratically with the area (for more details, see Section S1-A of the supplementary material).

B. Fabrication

Two different prototypes were built and characterized (see Fig. 1). The former results in a single-layer (SL) skin with 10:1 ratio of PDMS base to curing agent, whereas the latter has a GS with 10:1, 15:1, 20:1, and 30:1 layers of PDMS [53]. The Young's modulus of the different layers is 2.6, 1.7, 1.1, and 0.6



(a)



(b)

Fig. 2. (a) Prototypes comprising the PDMS layers and the flexible PCBs at the periphery. (b) Highlight of the 24 PEs and 24 PRs placed at the border of the sensing area and virtual grid. Solid lines represent the 8×8 grid, while dashed lines further divide the area into a 16×16 grid.

MPa. The SL design resembles the one used in [39], whereas the GS is a new design introduced in this article.

These configurations were studied in simulations by COMSOL Multiphysics, and more details can be found in Section S2 of the supplementary material.

In both cases, the 10:1 ratio allows a good bonding with the electronics located at the bottom side of the skin. Four flexible PCBs are placed at the bottom part of each mold. The elastomeric substrate of each prototype is prepared by mixing the crosslinker with the base monomer and degassing in vacuum. The PDMS is poured out, and the active components are embedded in the polymer with their connections on the outside. The fabrication of the prototype with GS is performed by casting the layers with the chosen crosslinker/base monomer ratios in successive iterations, after the previous polymer has partially cured for about one day at room temperature. In this way, the different layers result perfectly bonded. Fig. 2(a) shows two samples with a circular and square geometry, respectively.

C. Experimental Protocol

The experiments were conducted under the assumption that the PRs adequately filter ambient light and that objects of similar refractive index produce negligible differences in optical response when making contact with MSOWS surface. As

anticipated, the optical components are distributed along the skin boundary, and there is no wiring to the tactile units in the sensing area. The DAQ methods and experimental setup are described in the following.

The DAQ board consists of a custom printed circuit module with a field-programmable gate array (FPGA) (MyiR ZTurn 7020). The FPGA can activate the 24 input channels and synchronously read from 24 output channels from an analog-to-digital converter (ADC) with a 12-bit resolution. The internal scanning sequencer is directly interfaced with the on-chip direct memory access to transmit the readout data to the RT microcontroller, which, in turn, transfers user data protocol (UDP) packets to the host computer via an Ethernet connection. The output stream is then recorded using a LabVIEW interface. MATLAB (The MathWorks, Inc., Natick, MA, USA) is used for offline processing. The raw signals are normalized so that the resulting quantities are adimensional.

One major concern of optical-based technologies is the energy needed to power up the system. This issue was addressed by activating the PEs sequentially for enough time for the output signals to stabilize. The transient causes a time delay of the external readout circuitry; therefore, we identified a 2-ms activation time as a good tradeoff between stability and energy consumption. The sequential activation of the PEs is captured as a periodic signal of 168 samples for each of the 24 PRs, i.e., seven samples per PE activation. The last sample retains the informative content. Its variations over time are caused by a change in the optical path within the relative PR's cone of emission. A period of the signal is compressed into a 24×24 interaction matrix, whose elements are the seventh sample of the activations of the 24 PEs recorded by the 24 PRs. The size of this interaction matrix only depends on the number of PEs and PRs, and it is not related to what is in contact with the skin surface. This is a good representation since it resembles the mutual interactions among the components.

The virtual grid represented in Fig. 2(b) was defined to have a repeatable DAQ protocol. For both the geometries, bold lines identify the 8×8 primary grid, while dashed lines account for a further division into a 16×16 grid. Preliminary measurements showed four concentric zones [highlighted by different colors in Fig. 2(b)] having slight variations in the optical signal.

The primary grid was used to carry out indentation tests to obtain the pressure/indentation curve for the different zones. The MSOWS was characterized by using the experimental setup shown in Fig. 3. A vertical force is applied to the skin and measured through a triaxial load cell (ATI Nano 17, ATI Industrial Automation, Inc., Apex, NC, USA) interfaced to a Delrin probe that is brought to complete contact on each cell surface. Data are captured by a DAQ (USB-6218, National Instruments, Austin, TX, USA). A rigid support (upper layer in Delrin, pods in aluminum) keeps the skin in position so that the probe exerts a uniform pressure. Three orthogonal manual micrometric translation stages (M-105.10, Physik Instrumente, Karlsruhe, Germany) allow a manual positioning, followed by a micrometric servo-controlled translation stage (M-111.1DG, Physik Instrumente, Karlsruhe, Germany). The protocol for the acquisitions starts by bringing the motor to the highest vertical

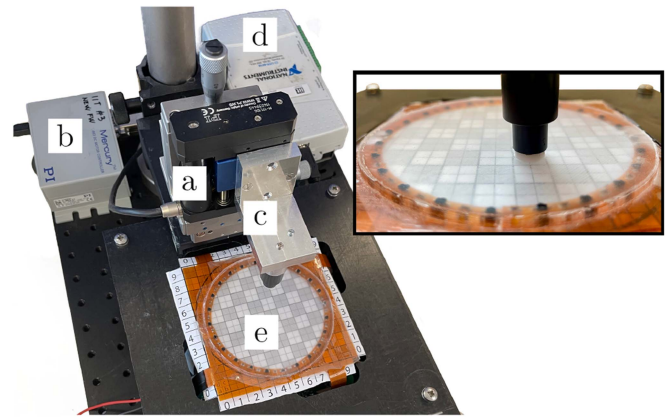


Fig. 3. Experimental setup loading system integrating: (a) the three orthogonal manual micrometric translation stages; (b) the servo-controlled micrometric translation stage; (c) the triaxial load cell connected to a squared Delrin probe; (d) DAQ to acquire data from the load cell; and (e) MSOWS prototype with a zoom on the probe in the top-right part of the image.

position. The communication with the hardware peripherals is then initialized. The vertical position is controlled via software, such that each acquisition starts at the same probe–skin distance. Each cell of the skin was indented by 2 mm for three cycles. Each time a new sample from the UDP stream is available, the load cell's value and the linear stage positions are recorded.

The two grid sizes were chosen to test different resolutions for contact location. A further increase in resolution was not addressed in this article because the number of cells scales quadratically with the division, resulting in a time-consuming testing procedure. Moreover, spatial resolution (SR) is limited by the number of sensing elements, the cone of optical signal emission/reception, and the miniaturization of the optoelectronic components.

D. Processing of the Tactile Information

The reconstruction process was divided into two steps: the study of a contact map and the estimation of the pressure exerted on the surface.

1) *Pattern-Recognition-Based Contact Map*: A pattern recognition algorithm was developed to obtain the skin multitouch capability. A pressure of 100 kPa is applied to each cell. An increment of at least 5% of the optical signal is set as the threshold to transform the interaction matrix into a Boolean pattern matrix. This procedure results in k 24×24 pattern matrices C_k , where $k = 64$ 256 is the number of cells. The true elements of the pattern matrix C_k identify the active PE–PR couples. Fig. 4 shows the matrices of a 16×16 grid division with a zoom on one of the cells. Each blue pixel corresponds to a PR whose response varies when the stimulation is applied, and the corresponding PE is active. The SR of the 16×16 grid is 5 mm, which is half the value obtained earlier in [39].

The interaction matrix O represents the current state of the sensor. The matching percentage of each cell a_k is the probability of that cell to be active in O . It is the elementwise multiplication

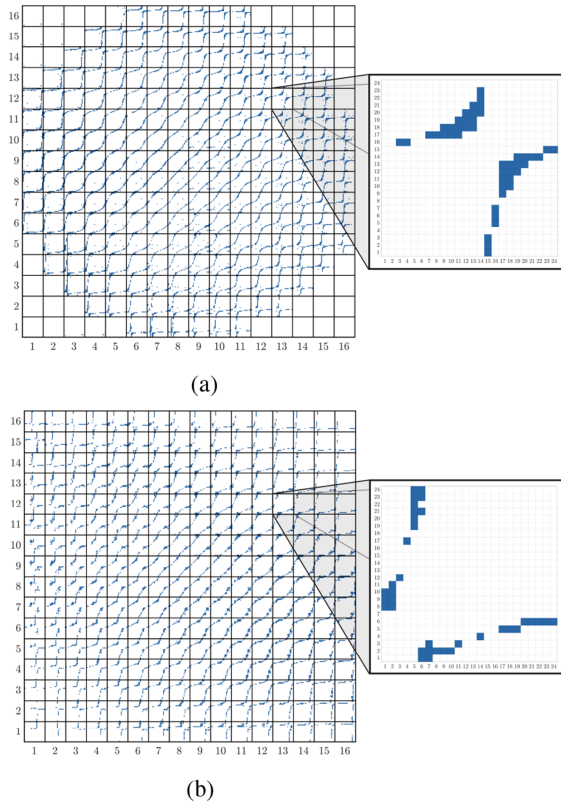


Fig. 4. 256 cells identified by the division of the sensing area into a 16×16 grid. The 24×24 pattern matrix is reported on top of each cell. Each pixel in the small squares represents a PE–PR couple. Blue pixels are ON, and white pixels are OFF. (a) Patterns of the circle sensor. (b) Patterns of the square sensor.

of O and the pattern of each cell C_k , divided by the number of active elements in that configuration. The division accounts for the number of true elements in the pattern matrix, which is not fixed among cells

$$a_k = \frac{O \cdot C_k}{\sum_{i=1}^{24} \sum_{j=1}^{24} C_{k,i,j}} \quad (1)$$

where i and j are the indices of rows and columns of the pattern matrices ranging from 1 to 24, as the number of electronic components. The probability of a touch event on each cell p_k is calculated by applying the SoftMax function [54] scaled by a factor $s = 0.01$. The standard exponential function is computed for each matching percentage a_k , and the sum of the exponentials normalizes these values

$$p_k = \frac{e^{-\frac{a_k - \max(a_k)}{s}}}{\sum_j e^{-\frac{a_j - \max(a_j)}{s}}} \quad (2)$$

The probability distribution of touch events over the sensing area is given by the probabilities of the cells to be active, which sum to 1. The parameter s balances between selectivity and predominance when computing the activation probability for multitouch detection. Indeed, an extremely small value would

result in an extremely high selectivity that could negatively affect the reconstruction when many cells are activated at once. When many cells are activated at once and $s \rightarrow 0$, the value of the cell corresponding to the strongest stimulus tends to 1 and goes to zero elsewhere. Conversely, when $s \rightarrow +\infty$, all the cells are given the same probability $1/n$.

2) Pressure Estimate: Since the cone of emission of the PEs is 60° , each PE is directly enlightened by the five opposite PRs. Hence, a 5×24 submatrix of the interaction matrix was considered to retain the overall pressure information. After the activation of each PE, the corresponding 5×1 column $O_{:,j}$ is updated. The optical output signal is calculated through the weighted average of $O_{:,j}$.

A built-in fault-tolerant mechanism is integrated by adjusting the weights to filter out disturbances due to temporary (e.g., a loose connection) and consistent errors (e.g., the damage of the soldermask defined pad pads of PCBs). Since both these conditions are not predictable, this effect was artificially elaborated by replacing the signal of some channels with the one obtained when there was a temporary problem at the connection. The standard deviation of well-functioning receivers is stable over time. On the one hand, a malfunctioning component has a low-value response with low variations or very abrupt changes. When any of these conditions occurs, the weight of that channel is lowered for the upcoming processing steps not to be affected. The response history of each PR is stored in memory. If there is a variation higher than 20% of the mean value of the history of standard deviations, or if their value is comparable to the resolution of the ADC, the weight associated with a specific PR is given a value of 0.05 (this value was obtained by a trial-and-error procedure). On the other hand, well-functioning PRs are equally weighted such that the five contributions sum to 1. Thus, the weights w_i of the weight matrix W are given according to

$$w_i = \begin{cases} 0.05, & \text{if } |\sigma_{PR_i} - \bar{\sigma}_{PR}| < Th \\ \frac{1 - 0.05Q}{5 - Q}, & \text{otherwise} \end{cases} \quad (3)$$

where σ_{PR_i} is the current standard deviation of a given PR, $\bar{\sigma}_{PR}$ is the average standard deviation over the last 24 activations, and Q is the number of malfunctioning PRs. Once the weights have been computed, the weighted sum of the input for each PE's activation is a new incoming optical output's value o

$$o = W \cdot O_{:,j}. \quad (4)$$

W can be seen as a spatial filter, which does not influence the signal when every PR is correctly working. The characterization of the sensor consisted in mapping the optical output to the overall pressure. A linear fitting is used first for the SL prototype. The parameters were identified for the zones reported in Fig. 2(b). In the GS prototype, a stepwise fitting is used to obtain a larger sensitivity for pressures lower than 10 kPa without reducing the sensing range. Higher pressure levels are retrieved by summing the maximum value of the linear tract with the output of a machine learning approach based on a time-delay neural network (TDNN). Indeed, the current value depends on both the newest update and the last activation of each PE, i.e., on the last 24 outputs. The architecture reported in Fig. 5 comprises

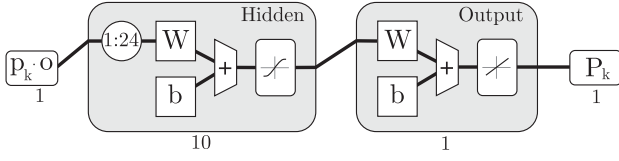


Fig. 5. Network architecture. The optical output o and the previous 24 time steps are the inputs of the network. The hidden layers has ten neurons and Bayesian regularization back-propagation. The output layer returns the estimated pressure value P_k for cell k .

one input layer, 24 input delays, and ten hidden neurons in the hidden layer.

The dataset used for training and testing was built by concatenating optical value sequences for a total amount of 774 930 samples. Two-third of these data were used to build the dataset for the training. More details can be found in Section S4 of the supplementary material. A validation set was not used because the training function implemented a Bayesian regularization. The offset related to the linear tract of the response is subtracted to the training and test data. The function g_k combines the first linear tract and the TDNN corrected by the offset value.

Given the probability distribution of touch events p_k (2) and the optical output o (4), an online algorithm that combines these results was implemented to retrieve the pressure map.

The elementwise product gives the partial distributions of the optical output. The pressure map is obtained by applying the function g_k cellwise. Then, the overall pressure P is computed by summing the elements of the pressure map

$$P = \sum_{k=1}^N P_k = \sum_{k=1}^N g_k(p_k \cdot o). \quad (5)$$

E. Multitouch Evaluation

The proposed criterion is valid to evaluate both the single- and multitouch events, and it is particularly suitable for ill-posed problems without a one-to-one correspondence between sensing elements and contact points. In the following, a measure for the reconstruction error is derived from a known contact map, its SR, and the ground truth. This error is then used in a test to estimate the error in the reconstruction of a pressure map.

1) **Contact Map Reconstruction Error (CMRE):** The sensing area is described by a target matrix T and a reconstructed matrix R , such that

$$T, R \in \mathbb{R}^{N \times M}.$$

These matrices represent the reconstruction map of the algorithm and the target map known *a priori*. The function f maps the point-by-point difference between the two matrices

$$f: [-1, 1] \times [0, 1] \rightarrow [0, 1] \\ f(R, T) = C = \tanh 3.5 (R - T)^2. \quad (6)$$

where the constant value 3.5 was chosen so that the saturation level reaches one. The nonzero elements of the matrix represent the contact points of T . The reconstruction error is given by two contributions: first, the contribution of the contact points, which represents how well the points that were touched have

been identified; second, the contribution of points not directly activated in the target map. As detailed in the following, a weight matrix $W \in \mathbb{R}^{N \times M}$ is computed to consider the aforementioned aspects:

$$W_{i,j} = \begin{cases} \frac{1}{N_c}, & i = x_c \wedge j = y_c \\ -\frac{1}{N_c \left(\left(\frac{SR}{35} \right)^2 + \sqrt{(i-x_c)^2 + (j-y_c)^2} \right)^2}, & i \neq x_c \wedge j \neq y_c \end{cases} \quad (7)$$

If the Cartesian coordinates $(i, j) \in \mathbb{N}$ are both equal to the coordinates of a contact point $(x_c, y_c) \in T$, then $W_{i,j}$ is given a value equal to the reciprocal of the total number of contact points. If the true contact points and the reconstructed points coincide, the overall error tends to zero; otherwise, it goes toward 1. If $(i, j) \neq (x_c, y_c)$, $W_{i,j}$ is given a negative weight proportional to the reciprocal of the distance from the closest point. This means that reconstructions close to the real point have the effect of mitigating the error (see Section S3 of the supplementary material).

The contribution of proximal cells is scaled according to the SR of the sensor, which considers the spatial distance between adjacent elements of T . When N_c contact points are present, the grid is clustered according to the most influent point. Each point (i, j) is given the minimum value among the N_c possibilities, i.e., $W = \min_{N_c}(w_{i,j,N_c})$. The overall reconstruction error is obtained by summing the contributions of each element $C_{i,j}$ scaled by the distance weight $W_{i,j}$

$$\text{CMRE} = \sum_{i=1}^N \sum_{j=1}^M W_{i,j} \cdot C_{i,j}. \quad (8)$$

2) **Pressure Map Test:** The test is computed by evaluating the CMRE when stimulating each contact point individually for different pressure levels. The global error is given by the average of each reconstruction point. The algorithm is shown in the following.

Algorithm 1: Pseudocode for the Pressure Map Test. For Each Point of the Skin, the CMRE Is Calculated for the Target Map and the Contact Map at Different Pressure Levels.

```

foreach raw element  $i = 1, \dots, N$  do
  foreach column element  $j = 1, \dots, M$  do
     $T(i, j) = 1$ , zero elsewhere
    foreach pressure level  $p = 1, \dots, P$  do
      Calculate the CMRE:  $E_{i,j,p} = \text{CMRE}(M, T)$ 
    Calculate the global error:
     $GE = \sum_{p=1}^P \sum_{i=1}^N \sum_{j=1}^M E_{i,j,p}$ 

```

III. RESULTS

In the following, a comparison between SL and GS skins is reported for the circular MSOWS. Then, the reconstruction with the two geometries is compared and analyzed.

A. Characterization of the SL and GS Skins

The circular prototype was tested on both the flat and curved surfaces with radii of curvature of 123.5, 61.7, and 30.9 mm,

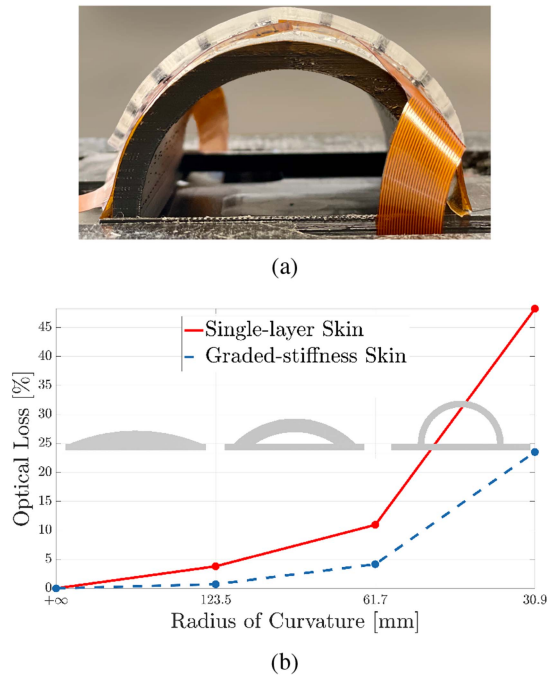


Fig. 6. MSOWS was put on surfaces with an increasing radius of curvature. (a) Surface with $\phi = 30.85$ mm. (b) Optical loss for surfaces with $\phi = 123.5, 61.7, 30.9$ mm.

respectively. Changes in the optical signal were retrieved by measuring the optical output, and data were compared to the outputs of the circular MSOWS positioned on a flat surface. Fig. 6 shows that the system can withstand a bending range up to 61.7 mm without compromising its functioning. Besides, the loss of optical power at the PR level of the GS prototype is consistently lower than that of the SL prototype.

The estimated pressure is reported for both the SL and the GS prototypes with and without the use of the TDNN. The optical output variations of the SL prototype are one order of magnitude smaller than those of the GS prototype. Fig. 7(a) shows that the maximum perceived pressure decreases from 254 kPa near the center of the sensing area to 213 kPa when approaching its periphery. The sensitivity ranges between 17.0 and 9.7 kPa⁻¹. The average hysteresis error is 33.35%, and the reconstruction error reaches 50% of the full-scale output (FSO). In the case of the GS skin, a stepwise fitting with two linear parts jointed by a second-order polynomial was used, as reported in Fig. 7(c).

The output of the TDNN has an MSE lower than 0.02 (see Section S4 of the supplementary material). Its combination with the stepwise fitting allows us to identify an FSO of 230 ± 3 kPa, with a negligible difference between the center and the periphery [see Fig. 7(d)]. At the same time, the hysteresis dropped to less than 0.1% on average, and the overall error was under 2.6%.

B. Pressure Estimate for the Circle and Square MSOWSs

The hysteretic behavior was compensated by the integration of the TDNN. Fig. 7(b) and (d) highlights that the reconstruction

can follow both the ascending and the descending curves. The hysteresis compensation can be clearly noticed in Fig. 8. The measured and estimated pressure values are reported in case of the circle and square GS prototypes. An additional evaluation on online data is reported in the supplementary information (see Section S7).

A fault-tolerant mechanism was implemented to reduce errors due to malfunctioning channels. The pressure value was calculated with the signal generated by randomly deactivating the channels. The number of channels to be deactivated was sequentially increased from 1 to 24. Each time, ten random combinations were selected, and the optical output was computed with fault tolerance both enabled and disabled.

The reconstruction error shown in Fig. 9 shows a slow increasing behavior. The output tends to a constant value when the number of deactivated channels increases. It is noteworthy that MSOWS shows the same performance, either when the fault-tolerant mechanism is enabled and half of the total components (i.e., 12) are not active or when only three components are not active and the mechanism is disabled.

The online pressure map was computed with the value $s=0.01$. It was chosen as the largest value before an error increase, as shown in Fig. 10(a). By applying the pressure map test reported in Algorithm 1 (see Section II-E), a global error of (1.87 ± 0.43) and $(1.67 \pm 0.23)\%$ was obtained for the circular and square prototype, respectively, when evaluated at 50 kPa. The CMRE for all the pressure levels is shown in Fig. 10(b). Moreover, the response for two-point contact was tested for points at 5-, 10-, and 20-mm distances, as reported in the supplementary information (see Section S7). The error going from the center toward the periphery is 1.75, 2.44, 1.88, and 1.40% for the circular case and 1.53, 2.01, 1.59, and 1.53% for the square case. In Fig. 11, images of the circular prototype under evaluation are shown. A video is also provided in the supplementary material (see Section S5) to highlight the capabilities of both the circular and square MSOWSs.

IV. CONCLUSION

The MSOWS was developed (based on a previously presented concept [39]) with tuned mechanical properties and a new pressure map algorithm. Pressure was estimated by exploiting the information contained in the last activation period. Overall, this approach dramatically boosts the performance by retrieving the pressure information for the whole surface with the same TDNN, independently of the stimulus's location. Moreover, this system can operate on bent surfaces with the radius of curvature ranging from 123.5 to 30.9 mm. The gradient stiffness was developed after studying the behavior in preliminary finite-element method simulations. The GS skin showed improved performance with respect to the SL skin in terms of signal intensity and pressure measurement errors. As described, by touching a cell of the virtual grid locally, changes of the external medium occur, and the refraction index varies accordingly. A limitation of the current system is that when this phenomenon occurs close to the MSOWS boundary, it affects the optical output since part of the optical rays from the PEs near the contact cell are

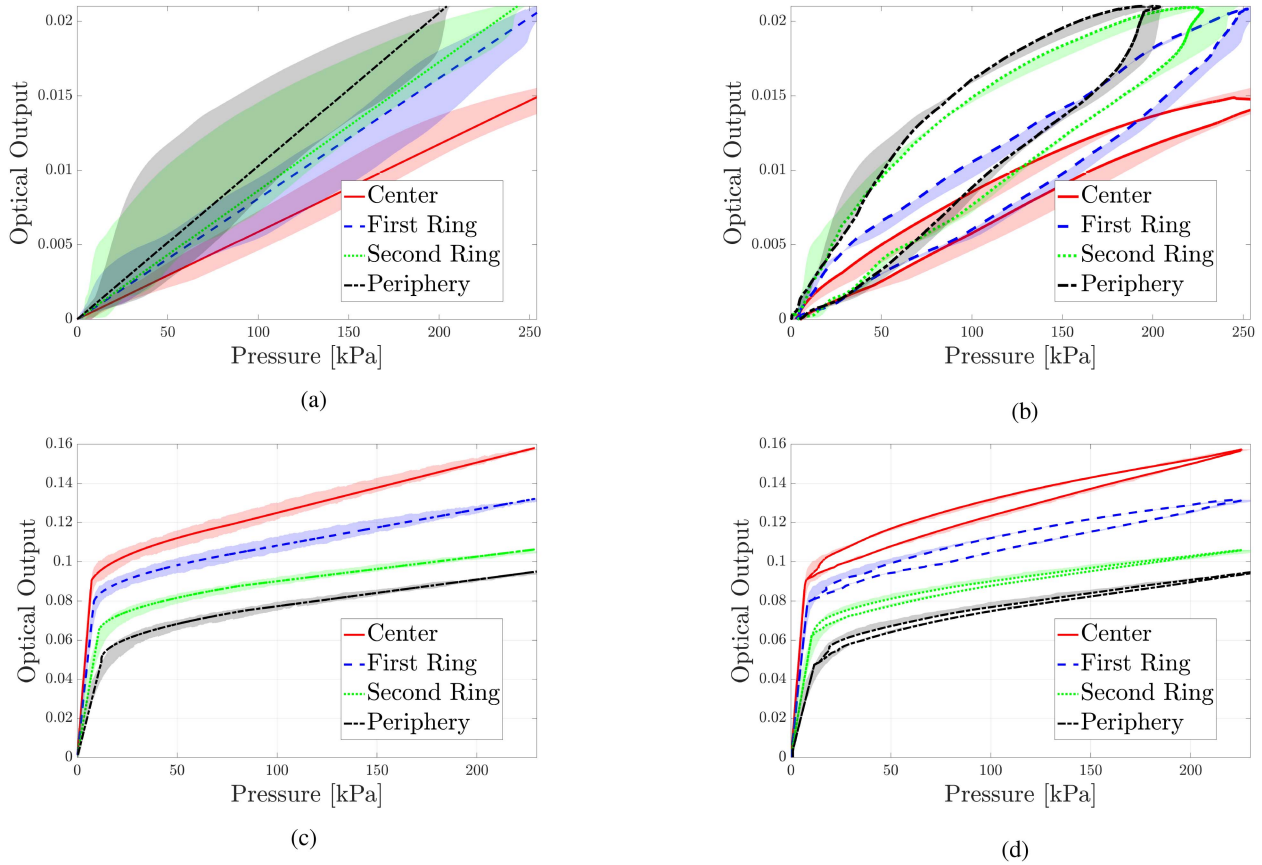


Fig. 7. Different fittings to map the optical output to the pressure in the different zones of the circular MSOWS. The SL prototype in (a) and (b) has low optical output values and large standard deviation. The optical signal is greatly improved in (c). The behavior for low and high pressure ranges can also be observed. The TDNN uses as inputs the newest optical data and the previous activation period, combined with the fittings. The effect of the TDNN is shown in (b) and (d). The overall standard deviation decreases, and the effect of the hysteresis is effectively compensated. (a) Linear fitting in the SL MSOWS. (b) Linear fitting and TDNN in the SL MSOWS. (c) Stepwise fitting in the GS MSOWS. (d) Stepwise fitting and TDNN in the GS MSOWS.

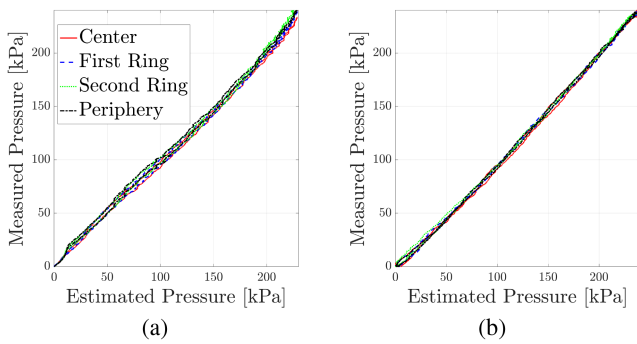


Fig. 8. Reconstructed and measured pressure. The hysteresis is effectively compensated in every part of the sensing area. (a) Circle skin. (b) Square skin.

backscattered to the adjacent PRs. Thus, the signal is attenuated at the informative side and has spurious increases when the PEs in front of the affected PRs are active. The GS skin design allows mitigating the above issue. Signal variations due to mechanical deformations are amplified, whereas the effect due to differences in the refraction index at the interface remains unaltered. This

latter effect is mildly mitigated by the ambient noise shields of the PEs and PRs. However, the attenuation is not enough, and we are currently working on an NIR thin coating, which is expected to improve the applicability of the sensor without affecting its soft tactile properties.

From previous works on optical sensing, EIT-based [30] and machine-learning-based single-touch [39] offline reconstructions were investigated. The major contribution of this article is to define a data processing workflow for online and multitouch distributed sensing. Indeed, the proposed approach has a lower dependence on the spatial arrangement of the sensing components with respect to EIT. It is noteworthy that the developed software allows for an online pressure map with hysteresis compensation and fault-tolerant mechanism. The combinations of GS and TDNN mitigated soft material's relaxation and nonlinearities, which are common in soft skins. **Table II** summarizes the results with the different approaches in this article.

The frame rate of the sensor is given by the update rate of the interaction matrix. A complete update occurs every 48 ms, so the frame rate is 21 Hz. However, every partial update (each 2 ms) is used to update the overall interaction matrix. The current

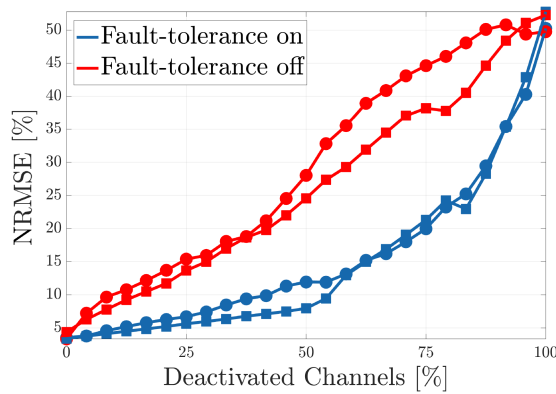


Fig. 9. Variation of the skin error with the percentage of malfunctioning channels, simulated by increasingly inactivating a random number of channels. The lines with the circular marker refer to the circle prototype, whereas the lines with the square marker refer to the square prototype. The error is normalized with respect to the FSO and evaluated on cyclic trajectories.

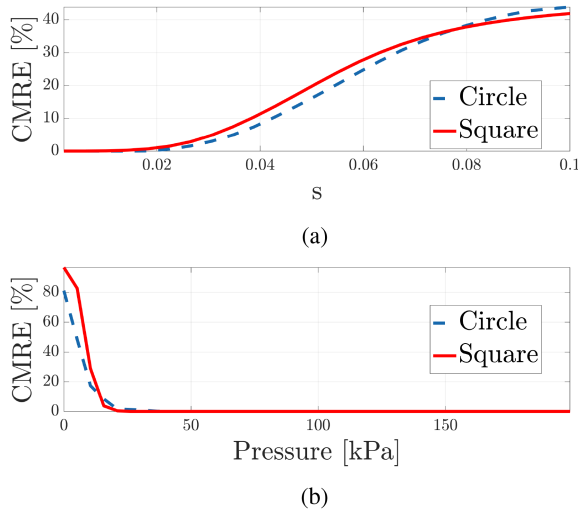


Fig. 10. (a) Average CMRE between the target and the reconstructed cells is computed for different scaling factors s to find the tradeoff between selectivity and predominance. (b) CMRE when varying the pressure level.

TABLE II
SUMMARY OF THE CHARACTERIZATION

	SL	SL+TDNN	GS	GS+TDNN
FSO [kPa]		234.7		230.5
Sensitivity [1/kPa]		13.4		LP: 8275.5 HP: 178.6
Hysteresis [%]	30.3	9.6	7.1	0.1
RMSE [%]	52.0	13.0	4.7	2.6

SL: SL skin, GS: GS skin, TDNN: result combined with the TDNN. LP and HP stand for pressure values under and above 10 kPa, respectively.

bottleneck is in the signal generation, since the algorithm was tested to take $(400 \pm 120) \mu\text{s}$ on a host computer without dedicated hardware. Thus, future plans consist in strongly decreasing this update time by optimizing the FPGA programming and the communication to an RT controller.

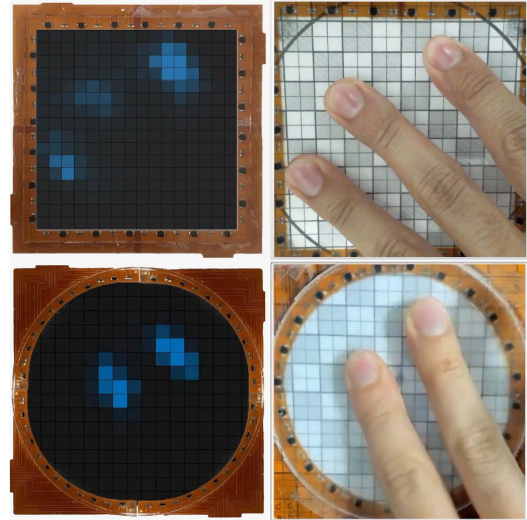


Fig. 11. Online pressure map reconstruction with the circular and square prototypes, where the partial pressures can be retrieved at cellwise level.

A limitation of the algorithm is the error for low-pressure values, as highlighted in Fig. 10(b). High error for no contact comes from the fact that every cell is given the same value. Nevertheless, the pressure map is scaled by the overall pressure value, and the resulting values are coherent. Future work will concentrate on low-pressure stimuli with an adaptive s parameter to increase the robustness of the reconstruction.

The contact map has been retrieved from both the circular and square prototypes. The pattern recognition framework is virtually independent of the arrangement of the sensing elements. What changes with the geometry is the actual pattern of the cells. The preliminary investigations on different shapes and reliability on bent surfaces are encouraging. Both the results and the highlighted limitations may be a valuable starting point toward multitouch and shape-independent reconstruction in soft optical skins.

Innovative soft sensing technologies must be low-cost and configurable into different shapes and sizes for various human-machine interfaces [55]. In this article, we propose a workflow for overall pressure estimation, contact map identification, and pressure map retrieval that can be virtually applied to every convex shape. In fact, every spatial arrangement of the PEs and PRs produces an offset activation matrix that is unique. The recognition of known sensor shapes can, hence, be automated. Having a high resistance to noise and wiring requirements up to the sensing area periphery, MSOWS allows a fast and reliable online reconstruction of multiple pressure stimuli within a dynamic range greater than 200 kPa per cell.

The approach presented in this article opens new possibilities for retrieving distributed tactile information without a physical array layout, regardless of the shape of the sensitive area. The obtained results demonstrate that by leveraging new signal processing strategies, like machine learning, and by coupling them with soft continuum optical waveguides, new generations

of intelligent tactile systems can be developed, holding strong potential for integration into robotic systems.

IV. ACKNOWLEDGMENT

The authors would like to thank C. Lorini, Electronic Design Laboratory, Istituto Italiano di Tecnologia, for his support in the development of the electronic system.

REFERENCES

- [1] W. Chen, H. Khamis, I. Birznieks, N. F. Lepora, and S. J. Redmond, "Tactile sensors for friction estimation and incipient slip detection—toward dexterous robotic manipulation: A review," *IEEE Sens. J.*, vol. 18, no. 22, pp. 9049–9064, Nov. 2018.
- [2] E. Torres-Jara and L. Natale, "Sensitive manipulation: Manipulation through tactile feedback," *Int. J. Humanoid Robot.*, vol. 15, no. 1, Feb. 2018, Art. no. 1850012.
- [3] T. G. Thuruthel, B. Shih, C. Laschi, and M. T. Tolley, "Soft robot perception using embedded soft sensors and recurrent neural networks," *Sci. Robot.*, vol. 4, no. 26, 2019, Art. no. eaav 1488.
- [4] K.-U. Kyung and S.-Y. Kim, "Soft sensors and actuators for designing new human-robot/machine interaction interfaces," in *Proc. 14th ACM/IEEE Int. Conf. Human-Robot Interact.*, 2019, pp. 695–695.
- [5] T. Arnold and M. Scheutz, "The tactile ethics of soft robotics: Designing wisely for human-robot interaction," *Soft Robot.*, vol. 4, no. 2, pp. 81–87, Jun. 2017.
- [6] S. Zhang, S. Li, Z. Xia, and K. Cai, "A review of electronic skin: Soft electronics and sensors for human health," *J. Mater. Chem. B*, vol. 8, no. 5, pp. 852–862, 2020.
- [7] H. Zhao, K. O'Brien, S. Li, and R. F. Shepherd, "Optoelectronically innervated soft prosthetic hand via stretchable optical waveguides," *Sci. Robot.*, vol. 1, no. 1, 2016, Art. no. eaai7529.
- [8] G. Cheng, E. Dean-Leon, F. Bergner, J. R. G. Olvera, Q. Leboutet, and P. Mittendorf, "A comprehensive realization of robot skin: Sensors, sensing, control, and applications," *Proc. IEEE*, vol. 107, no. 10, pp. 2034–2051, Oct. 2019.
- [9] J. C. Yang, J. Mun, S. Y. Kwon, S. Park, Z. Bao, and S. Park, "Electronic skin: Recent progress and future prospects for skin-attachable devices for health monitoring, robotics, and prosthetics," *Adv. Mater.*, vol. 31, no. 48, 2019, Art. no. 1904765.
- [10] T. Hellebrekers, O. Kroemer, and C. Majidi, "Soft magnetic skin for continuous deformation sensing," *Adv. Intell. Syst.*, vol. 1, no. 4, 2019, Art. no. 1900025.
- [11] W. Schiff and E. Foulke, *Tactual Perception: A Sourcebook*. Cambridge, U.K.: Cambridge Univ. Press, 1982.
- [12] J. Xu et al., "Highly stretchable polymer semiconductor films through the nanoconfinement effect," *Science*, vol. 355, no. 6320, pp. 59–64, 2017.
- [13] T. T. Tung, C. Robert, M. Castro, J. F. Feller, T. Y. Kim, and K. S. Suh, "Enhancing the sensitivity of graphene/polyurethane nanocomposite flexible piezo-resistive pressure sensors with magnetite nano-spacers," *Carbon*, vol. 108, pp. 450–460, 2016.
- [14] Y. F. Fu et al., "Super soft but strong E-skin based on carbon fiber/carbon black/silicone composite: Truly mimicking tactile sensing and mechanical behavior of human skin," *Composites Sci. Technol.*, vol. 186, 2020, Art. no. 107910.
- [15] A. Rinaldi, A. Tamburrano, M. Fortunato, and M. S. Sarto, "A flexible and highly sensitive pressure sensor based on a PDMS foam coated with graphene nanoplatelets," *Sensors*, vol. 16, no. 12, 2016, Art. no. 2148.
- [16] P. S. Girão, P. M. P. Ramos, O. Postolache, and J. Miguel Dias Pereira, "Tactile sensors for robotic applications," *Measurement: J. Int. Meas. Confederation*, vol. 46, no. 3, pp. 1257–1271, 2013.
- [17] O. Atalay, A. Atalay, J. Gafford, H. Wang, R. Wood, and C. Walsh, "A highly stretchable capacitive-based strain sensor based on metal deposition and laser rastering," *Adv. Mater. Technol.*, vol. 2, no. 9, 2017, Art. no. 1700081.
- [18] O. Atalay, A. Atalay, J. Gafford, and C. Walsh, "A highly sensitive capacitive-based soft pressure sensor based on a conductive fabric and a microporous dielectric layer," *Adv. Mater. Technol.*, vol. 3, no. 1, 2018, Art. no. 1700237.
- [19] H. Wang, M. Totaro, and L. Beccai, "Development of fully shielded soft inductive tactile sensors," in *Proc. 26th IEEE Int. Conf. Electron., Circuits Syst.*, 2019, pp. 246–249.
- [20] S. Hamaguchi et al., "Soft inductive tactile sensor using flow-channel," *IEEE Robot. Autom. Lett.*, vol. 5, no. 3, pp. 4028–4034, Apr. 2020.
- [21] J. Rossiter and T. Mukai, "A novel tactile sensor using a matrix of LEDs operating in both photoemitter and photodetector modes," *Proc. IEEE SENSORS Conf.*, 2005, pp. 994–997.
- [22] P. A. Xu, A. K. Mishra, H. Bai, C. A. Aubin, L. Zullo, and R. F. Shepherd, "Optical lace for synthetic afferent neural networks," *Sci. Robot.*, vol. 4, no. 34, pp. 1–10, 2019.
- [23] J. Rossiter and T. Mukai, "An LED-based tactile sensor for multi-sensing over large areas," in *Proc. IEEE SENSORS Conf.*, 2006, pp. 835–838.
- [24] L. Massari et al., "A machine-learning-based approach to solve both contact location and force in soft material tactile sensors," *Soft Robot.*, vol. 7, no. 4, pp. 409–420, 2020.
- [25] M. I. Tiwana, S. J. Redmond, and N. H. Lovell, "A review of tactile sensing technologies with applications in biomedical engineering," *Sens. Actuators A: Phys.*, vol. 179, pp. 17–31, 2012.
- [26] R. S. Dahiya, G. Metta, M. Valle, and G. Sandini, "Tactile sensing—From humans to humanoids," *IEEE Trans. Robot.*, vol. 26, no. 1, pp. 1–20, Feb. 2010.
- [27] R. S. Dahiya and M. Valle, "Tactile sensing for robotic applications," in *Sensors: Focus on Tactile Force and Stress Sensors*. Rijeka, Croatia: InTech, 2008, pp. 298–304.
- [28] C. Lucarotti, C. Oddo, N. Vitiello, and M. Carrozza, "Synthetic and bio-artificial tactile sensing: A review," *Sensors*, vol. 13, no. 2, pp. 1435–1466, 2013.
- [29] H. Yousef, M. Boukallel, and K. Althoefer, "Tactile sensing for dexterous in-hand manipulation in robotics—A review," *Sens. Actuators A: Phys.*, vol. 167, no. 2, pp. 171–187, 2011.
- [30] A. Levi, M. Piovanelli, S. Furlan, B. Mazzolai, and L. Beccai, "Soft, transparent, electronic skin for distributed and multiple pressure sensing," *Sensors*, vol. 13, no. 5, pp. 6578–6604, 2013.
- [31] M. Zhu, T. He, and C. Lee, "Technologies toward next generation human machine interfaces: From machine learning enhanced tactile sensing to neuromorphic sensory systems," *Appl. Phys. Rev.*, vol. 7, no. 3, 2020, Art. no. 031305.
- [32] S. Russo, R. Assaf, N. Carbonaro, and A. Tognetti, "Touch position detection in electrical tomography tactile sensors through quadratic classifier," *IEEE Sens. J.*, vol. 19, no. 2, pp. 474–483, Jan. 2019.
- [33] E. Judd, K. M. Digumarti, J. Rossiter, and H. Hauser, "NeatSkin: A discrete impedance tomography skin sensor," *Proc. 3rd IEEE Int. Conf. Soft Robot.*, 2020, pp. 33–38.
- [34] K. Park, H. Park, H. Lee, S. Park, and J. Kim, "An ERT-based robotic skin with sparsely distributed electrodes: Structure, fabrication, and DNN-based signal processing," in *Proc. IEEE Int. Conf. Robot. Autom.*, 2020, pp. 1617–1624.
- [35] A. Adler et al., "GREIT: A unified approach to 2D linear EIT reconstruction of lung images," *Physiol. Meas.*, vol. 30, no. 6, 2009, Art. no. S35.
- [36] J. D. Kelleher, B. Mac Namee, and A. D'arcy, *Fundamentals of Machine Learning for Predictive Data Analytics: Algorithms, Worked Examples, and Case Studies*. Cambridge, MA, USA: MIT Press, 2015.
- [37] P. Cunningham, M. Cord, and S. J. Delany, "Supervised Learning," in *Machine Learning Techniques for Multimedia*. Berlin, Germany: Springer, 2008, pp. 21–49.
- [38] Y. Zhang, Z. Lin, X. Huang, X. You, J. Ye, and H. Wu, "A large-area, stretchable, textile-based tactile sensor," *Adv. Mater. Technol.*, vol. 5, no. 4, pp. 1–10, 2020.
- [39] D. O. Amoateng, M. Totaro, M. Crepaldi, E. Falotico, and L. Beccai, "Intelligent position, pressure and depth sensing in a soft optical waveguide skin," in *Proc. IEEE Int. Conf. Soft Robot.*, 2019, pp. 349–354.
- [40] K. Chin, T. Hellebrekers, and C. Majidi, "Machine learning for soft robotic sensing and control," *Adv. Intell. Syst.*, vol. 2, no. 6, 2020, Art. no. 1900171.
- [41] D. Kim et al., "Review of machine learning methods in soft robotics," *PLoS ONE*, vol. 16, no. 2, pp. 1–24, Feb. 2021.
- [42] H. Lee, H. Park, G. Serhat, H. Sun, and K. J. Kuchenbecker, "Calibrating a soft ERT-based tactile sensor with a multiphysics model and sim-to-real transfer learning," in *Proc. IEEE Int. Conf. Robot. Autom.*, 2020, pp. 1632–1638.
- [43] P. J. Vauhkonen, M. Vauhkonen, T. Savolainen, and J. P. Kaipio, "Three-dimensional electrical impedance tomography based on the complete electrode model," *IEEE Trans. Biomed. Eng.*, vol. 46, no. 9, pp. 1150–1160, Sep. 1999.
- [44] T. Zhao, C. Wu, and M. Soleimani, "Ionic liquid based distributed touch sensor using electrical impedance tomography," *IOP SciNotes*, vol. 1, no. 2, 2020, Art. no. 025005.

- [45] D. Liu, D. Smyl, D. Gu, and J. Du, "Shape-driven difference electrical impedance tomography," *IEEE Trans. Med. Imag.*, vol. 39, no. 12, pp. 3801–3812, Dec. 2020.
- [46] Z. Zhang and B. D. Rao, "Source vectors using sparse Bayesian learning," *IEEE J. Sel. Topics Signal Process.*, vol. 5, no. 5, pp. 912–926, Sep. 2011.
- [47] S. Liu, J. Jia, Y. D. Zhang, and Y. Yang, "Image reconstruction in electrical impedance tomography based on structure-aware sparse Bayesian learning," *IEEE Trans. Med. Imag.*, vol. 37, no. 9, pp. 2090–2102, Sep. 2018.
- [48] K. Liu *et al.*, "Artificial sensitive skin for robotics based on electrical impedance tomography," *Adv. Intell. Syst.*, vol. 2, no. 4, 2020, Art. no. 1900161.
- [49] O. Ronneberger, P. Fischer, and T. Brox, "U-net: Convolutional networks for biomedical image segmentation," in *Proc. Int. Conf. Med. Image Comput. Comput.- Assist. Intervention*, 2015, pp. 234–241.
- [50] J. A. Sánchez-Durán, Ö. Oballe-Peinado, J. Castellanos-Ramos, and F. Vidal-Verdú, "Hysteresis correction of tactile sensor response with a generalized Prandtl-Ishlinskii model," *Microsyst. Technol.*, vol. 18, no. 7/8, pp. 1127–1138, 2012.
- [51] H. S. Han, J. Yoon, S. Nam, S. Park, and D. J. Hyun, "A soft ground reaction force sensor system utilizing time-delay recurrent neural network," *IEEE Sens.*, vol. 20, no. 18, pp. 10851–10861, Sep. 2020.
- [52] M. Lo Preti, M. Totaro, E. Falotico, and L. Beccai, "Optical-based soft technologies for artificial tactile sensing," in *Electronic Skin: Sensors and Systems*, A. Ibrahim and M. Valle, Eds. Gistrup, Denmark: River Publishers, 2020, pp. 73–99.
- [53] Z. Wang, A. A. Volinsky, and N. D. Gallant, "Crosslinking effect on polydimethylsiloxane elastic modulus measured by custom-built compression instrument," *J. Appl. Polym. Sci.*, vol. 131, no. 22, pp. 1–4, 2014.
- [54] T. Burr, "Pattern recognition and machine learning," *J. Amer. Statist. Assoc.*, vol. 103, pp. 886–887, 2008.
- [55] W. Lee, Y. Kim, M. Y. Lee, J. H. Oh, and J. U. Lee, "Highly stretchable fiber transistors with all-stretchable electronic components and graphene hybrid electrodes," *Org. Electron.*, vol. 69, pp. 320–328, 2019.



Matteo Lo Preti received the B.Sc. degree in biomedical engineering from the University of Pisa, Pisa, Italy, in 2017, and the M.Sc. degree in bionics engineering from the University of Pisa jointly with Scuola Superiore Sant'Anna, Pisa, Italy, in 2019. He is currently working toward the Ph.D. degree in biorobotics with Scuola Superiore Sant'Anna with affiliation to the Istituto Italiano di Tecnologia, Genova, Italy, tutored by Dr. Lucia Beccai and under the supervision of Dr. Egidio Falotico.

His research interests include soft tactile sensing and tactile-based artificial intelligence.



Massimo Totaro (Member, IEEE) received the M.Sc. degree in electronics engineering and the Ph.D. degree in information engineering from the University of Pisa, Pisa, Italy, in 2006 and 2010, respectively. He is currently a Postdoctoral Fellow with the Istituto Italiano di Tecnologia, Genoa, Italy. He was a Postdoc with the University of Pisa, Pisa, Italy, focused on novel nanostructures based on silicon and heterostructures, for electronic sensing and thermoelectric applications. His research interests

mainly include modeling, fabrication and characterization of bioinspired tactile systems, wearable devices, soft robots, and micro or nanoelectronic components.



Egidio Falotico (Member, IEEE) received the dual Ph.D. degree in innovative technologies from Scuola Superiore Sant'Anna, Pisa, Italy, and in cognitive science from Pierre et Marie Curie University Paris, France, in 2013, and the M.Sc. degree in computer science from the University of Pisa, Pisa, Italy, in 2008. He is currently an Assistant Professor with the BioRobotics Institute, Scuola Superiore Sant'Anna.

Since his early studies, he has developed his strong interest in the domain of neuroscience and through his double Ph.D. degree, he had the chance to explore the potential of neuroscience knowledge applied to robotics. He works on different projects, such as RoboSoM and Human Brain Project with the BioRobotics Institute, Pontedera, Italy. In the framework of this last project, he is a co-leader of the Subproject10—Neurorobotics. Since 2017, he has been very active in the field of soft robotics, putting into practice his deep expertise in artificial intelligence and computational neuroscience for the control of soft robots.



Marco Crepaldi (Member, IEEE) received the M.S. and Ph.D. degrees in electrical engineering from the Politecnico di Torino (Polito), Turin, Italy, in 2005 and 2009, respectively.

He was a Postdoctoral Researcher with the VLSI-Lab, Department of Electrical Engineering, Polito. In 2008, he was a Visiting Scholar with Columbia University, New York, NY, USA, working with Professor Peter Kinget. He was a junior and then senior Postdoctoral Researcher with the Istituto Italiano di Tecnologia, Polito, Center for Space Human Robotics, Smart Materials Platform, from 2010 to mid-2016. He is currently the Coordinator of the Electronic Design Laboratory, Center for Human Technology, Istituto Italiano di Tecnologia, Genova, Italy. His research interests include CMOS ultralow-power ultrawideband transceiver design, VHDL-AMS behavioral modeling of analog mixed-signal circuits, wireless communications circuits and systems, ultralow-current amplifiers, sensing elements for nanostructures, and development of systems for professional digital video and audio broadcasting.



Lucia Beccai (Member, IEEE) received the graduation degree in electronic engineering from the University of Pisa, Pisa, Italy, and the Ph.D. degree in microsystem engineering from the University of Rome Tor Vergata Rome, Italy, in 2003. She is currently a Tenured Senior Researcher with the Istituto Italiano di Tecnologia, Genova, Italy, where she leads the Group Soft BioRobotic Perception. From 2003 to 2008, she was a Postdoctoral Fellow and until 2009 an Assistant Professor in biomedical engineering

with the Biorobotics Institute of Scuola Superiore Sant'Anna, Pisa, Italy. She has a long experience in bioinspired smart tactile systems and bionics. She filed three patents and has authored more than 100 articles on refereed international journals, books, and international conference proceedings. Her research interests include biorobotics and soft robotics fields with the final aim of achieving soft sensing and perceptive soft robotic solutions for intelligent and safe interaction with the environment and humans. Specific topics include, multimodal tactile systems inspired by natural mechanotransduction, soft robotic systems for active and passive touch, milli- and micro-scale fabrication technologies for 3D active structures, soft versatile grasping, and manipulation, and wearable soft sensing. She collaborated and had scientific responsibility in many international projects at European and intercontinental level. She is currently the Scientific Coordinator of the PROBOSCIS Project (EU H2020-FET Open 863212).